Influence of the Mn5Ge3/Ge ohmic-contact interface on the Seebeck coefficient of the Mn5Ge3/Ge bilayer

Alain Portavoce, Siham Hassak, Maxime Bertoglio

scientific reports

Check for updates

OPEN

Influence of the Mn_5Ge_3/Ge ohmic-contact interface on the Seebeck coefficient of the Mn_5Ge_3/Ge bilayer

Alain Portavoce✉, Siham Hassak & Maxime Bertoglio

Thermoelectricity is a well-known effect that can be used to convert heat energy into electrical energy. However, the yield of this conversion is still low compared to current photovoltaic technology. It is limited by the intrinsic properties of materials, leading to intensive materials science investigations for the design of efficient thermoelectric (TE) materials. Interface engineering was shown to be a valuable solution for improving materials' TE properties, supporting the development of multiphase TE materials. In particular, interfaces have been suggested to promote the increase of the Seebeck coefficient of materials without significantly impacting their electrical conductivity through the so-called energy filtering effect. This work aims at determining experimentally the effect of a metal/semiconductor interface exhibiting an ohmic character on the effective Seebeck coefficient of multiphase materials, focusing on the *n*-type Mn_5Ge_3/*p*-type Ge interface. This interface is shown not to contribute to carrier transport, but to contribute to carrier concentration filtering due to carrier injection or recombination. The Seebeck coefficient of the bi-phase material is shown to be dependent on the direction carriers are crossing the interface. The interface effect mainly results from a modification of charge carrier concentrations in the semiconductor.

Worldwide efforts for the development of efficient thermoelectric (TE) devices is motivated by their ability of safely produce electricity from waste heat without CO_2 production[1–4], theoretically ranking them among the best solutions for energy harvesting. However, their yield of converting waste heat into electrical power is still currently low (~ 10%) as it dependents on interrelated material properties exhibiting contrasting effects on TE properties[5–8]. Indeed, the conversion efficiency of a given TE material is determined by the figure of merit $ZT = T \times S^2\sigma/\kappa$ (T the absolute temperature, S the Seebeck coefficient, σ the electrical conductivity, and κ the thermal conductivity)[3,5–7]. Higher the ZT, higher the TE efficiency, meaning that efficient TE materials should exhibit high Seebeck coefficient, high electrical conductivity, and low thermal conductivity. However, S and σ are in general inversely proportional, and the electronic component of thermal conductivity increases with electrical conductivity, limiting the TE efficiency of materials in general.

Consequently, a wide material panel is being explored for TE power generation applications, including the compounds GeTe[9,10] and PbTe[11,12], and half-Heusler compounds[13], for example, aiming at discovering the most effective TE material. Though, multiphase materials were shown these past 10 years to exhibit higher ZT than single-phase materials[14–19], allowing to reach $ZT > 2$ in some cases[8,18,20–22], suggesting the possibility of reaching the limit $ZT = 3$, considered as the condition for the production of efficient devices, matching application requirements[1–3,5,23]. Usually, TE properties of multiphase materials are considered to be higher than single-phase materials due to the combination of increased phonon scattering at interfaces, increased Seebeck coefficient due to interface-mediated energy filtering, and increased electrical conductivity due to modulation doping. The effect of nanostructuration and nano-size phase inclusions on thermal conductivity has been directly proved thanks to heat conduction measurements[17,24–30], and interpreted as due to a modification of the phonon component of thermal conductivity[5–8,18,22,23,31,32], allowing the ZT numerator to be reduced. The increase of the power factor $PF = S^2\sigma$ (ZT denominator) in multiphase materials is often attributed to the effect of interfaces, in particular in the case of S increase, generally interpreted as the energy filtering effect of the interface between the matrix and inclusions[14,15,17–20,24,28,33,34] or grain boundaries[27,35–39].

IM2NP, Faculté des Sciences de Saint-Jérôme case 142, Aix-Marseille University/CNRS, 13397 Marseille, France. ✉email: alain.portavoce@im2np.fr

Despite theoretical models[37,39–42] and numerical calculations[18,43,44] showing a possible increase of S due to interface-mediated energy filtering, the effect of interfaces on S still needs further experimental investigations in order to improve TE property engineering of multiphase materials. For example, the dependence of S with interface area in multiphase materials exhibiting enhanced S has been poorly studied[45], and some experimental results shown no modification of S with the presence of interfaces[21,25,28,29,45–48]. Furthermore, the increase of S in multiphase materials has been shown as possibly due to a significant gradient of charge mobility resulting from the temperature gradient[49]. The junction between two conducting solids of very different charge carrier mobilities is thus expected to promote an increase of S that is not related to energy filtering of charge carriers.

The present study aims at probing the influence of a single interface on the effective Seebeck coefficient (S_{eff}) of a binary multiphase material, and to provide an experimental proof of Seebeck coefficient modification due to the interface. The experiments were performed around room temperature with complementary-metal–oxide–semiconductor (CMOS) compatible materials to match the requirements of CMOS-integrated TE device for energy harvesting in portable microelectronic circuits[50,51].

Interfaces in multiphase thermoelectric materials

TE materials are usually p- or n-type semiconductors[28,30,46,52–54], and Schottky contacts/interfaces between the semiconductor and a metallic phase is often considered as the main solution for interface-mediated energy filtering of charge carriers[18,37,40–42]. Figure 1a schematically presents the electronic band structure between a metallic phase and a p-type semiconductor, and Fig. 1b presents a schematic of a typical I–V curve of a Schottky contact. Due to the difference of Fermi level (E_F) between the two materials before contact, an energy barrier is built (for holes in the present example) close to the interface after contact. This barrier is expected to scatter carriers of low energy, reducing the number of free carriers and increasing their average energy, leading to the increase of S_{eff} (energy filtering effect)[18,40–42].

A second type of metal/semiconductor interface can be built, corresponding to an ohmic contact. No major barrier is present at the interface in this case (Fig. 1c), and charge carriers can cross the interface corresponding to the I-V curve schematic shown in Fig. 1d. This type of interface is usually considered as having no singular effect on S_{eff}. This is nevertheless this type of interface that the present work aims at investigating, since it has been poorly studied yet and can be considered as a reference to be compared with other metal/semiconductor interfaces.

The chosen interface is the contact between a polycrystalline thin film of the metallic compound Mn_5Ge_3 and a polycrystalline thin film of p-type Ge. Mn_5Ge_3 is known to be n-type[55] and to form an ohmic contact with Ge if Ge is p-type or a Schottky contact if Ge is n-type[56,57]. An n-type metal/p-type semiconductor interface allows possible carrier injection through the interface to be more easily evidenced. Mn and Ge were deposited at room temperature by magnetron sputtering on glass substrate[55,58], and the Mn_5Ge_3/Ge bilayer was grown by reactive diffusion thanks to ex situ annealing under vacuum ($P \sim 10^{-7}$ mbar) at 400 °C for 10 min[55,59,60]. The use of thin films allows the study of a single interface, as well as the volume of the phases to be precisely controlled. The

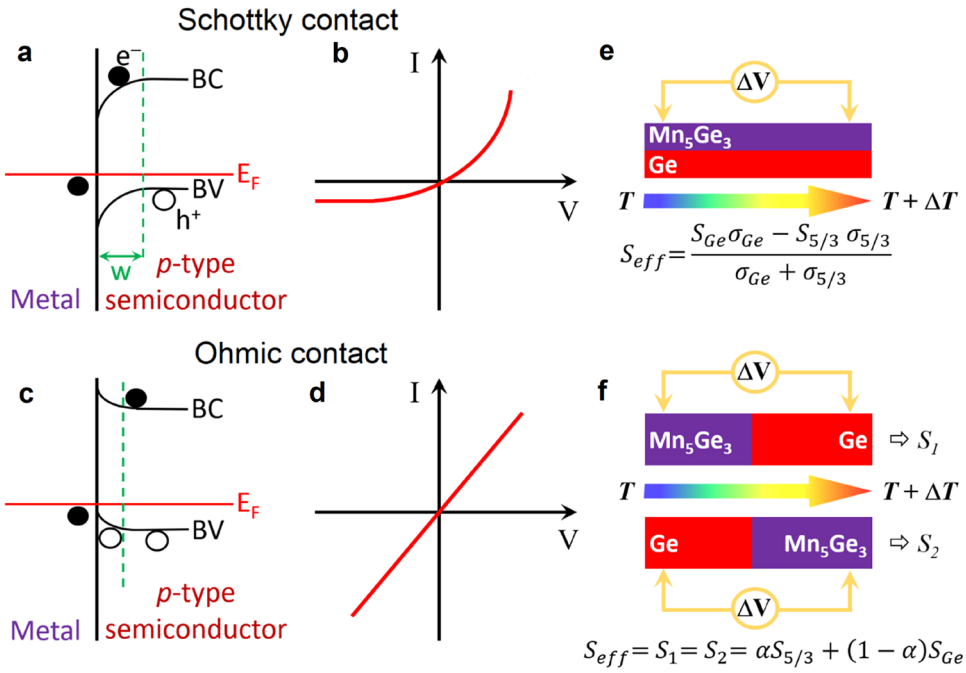

Figure 1. n-type metal/p-type semiconductor interfaces. Schematics of respectively the electronic band diagram and the I–V characteristics of a Schottky contact (**a**) and (**b**), and an ohmic contact (**c**) and (**d**). (**e**) and (**f**) show two types of interfaces between two materials (Mn_5Ge_3 and Ge) corresponding to parallel or serial charge carrier channels, respectively.

sputtering technique guaranty a control of the film thickness below 5 nm, as well as a low level of contamination, below 10^{19} cm^{-3} in our case[61]. Furthermore, structural and electrical characteristics of the Mn_5Ge_3/Ge interface is generally considered to be well reproducible through reactive diffusion fabrication[56,62,63].

The influence of an interface on the S_{eff} of multiphase materials can be probed through two types of geometry: (1) the parallel-phase geometry, and (2) the serial-phase geometry. In our case, the parallel-phase geometry corresponds to the Seebeck coefficient $S_{eff} = \Delta V/\Delta T$ measured on the bilayer Mn_5Ge_3/Ge according to Fig. 1e. This geometry corresponds to the model of two conduction channels in parallel along the temperature gradient. The charge carriers are moving in the direction parallel to the interface in the two materials. Electrons in Mn_5Ge_3 and holes in Ge are moving towards the cold side of the bilayer. As presented in Fig. 1e, S_{eff} should only depend in this case on the Seebeck coefficients (S_{Ge} and $S_{5/3}$) and the electrical conductivities (σ_{Ge} and $\sigma_{5/3}$) of each material Ge and Mn_5Ge_3 if the interface has no effect. However, due to carrier confinement or due to the formation of a third phase at the interface for example, the interface can act as an additional carrier channel. In this case, the signature of the interface effect can be detected in S_{eff}, as the equation given in Fig. 1e needs to be modified to take into account the Seebeck coefficient and the conductivity of this third channel located at the Mn_5Ge_3/Ge interface[16,44,47,64]. In the serial-phase geometry (Fig. 1f), the two materials in contact, Ge and Mn_5Ge_3, are placed in series in the temperature gradient: the charge carriers move perpendicularly to the interface in this case, and either electrons in Mn_5Ge_3 (S_2 in Fig. 1f) or holes in Ge (S_1 in Fig. 1f) move towards the interface if Ge or Mn_5Ge_3 are respectively located at the cold side. If the interface has no particular effect on carriers, S_{eff} should be equal to the sum of the two Seebeck coefficient S_{Ge} and $S_{5/3}$ weighted by the relative volume fraction of their corresponding phase Ge or Mn_5Ge_3 (coefficient α in Fig. 1f), and the effective Seebeck coefficients S_1 (measured with Ge at the hot side Fig. 1f) and S_2 (measured with Ge at the cold side Fig. 1f) should be identical. This geometry models the possible effects of GBs or precipitates on the effective Seebeck coefficient of multiphase materials. If the Mn_5Ge_3/Ge interface plays a role on charge carriers, the equation given in Fig. 1f would not be fulfilled and S_{eff} should vary depending on the position of Ge (and Mn_5Ge_3) in the temperature gradient (in the colder region or in the hotter region), exhibiting nonreciprocity versus the temperature gradient direction[65].

Mn_5Ge_3/Ge interface contribution to carrier transport

Figure 2a presents the electrical conductivity measured versus temperature (T) on a 100 nm-thick Ge (σ_{Ge}) film and on a 160 nm-thick Mn_5Ge_3 film ($\sigma_{5/3}$) deposited on glass substrate. σ_{Ge} increases with temperature, corresponding to a semiconductor behavior for Ge, while $\sigma_{5/3}$ decreases when the temperature increases, corresponding to a metallic behavior for Mn_5Ge_3, as expected. The conductivity is found to be about two orders of magnitude larger in the Mn_5Ge_3 metallic film compared to the Ge semiconductor film. Figure 2b presents two I–V curves characteristic of the studied Mn_5Ge_3/Ge contact. The measurements were performed according to the Van der Pauw method on a bilayer Mn_5Ge_3/Ge sample, after removing part of the Mn_5Ge_3 film by chemical etching, making a 160 nm-thick step between a Mn_5Ge_3 upper terrace and a Ge lower terrace (see inset in Fig. 2b). One measurement was performed positioning four Cu tips directly on the sample (black dashed line), and one measurement was performed using the same Cu tips but positioned on Al contacts evaporated on the sample through a mask (red solid line). The I–V curves correspond to an ohmic contact, as expected.

Figure 3a shows the Seebeck coefficients S_{Ge} (red open circles) of the 100 nm-thick Ge film and $S_{5/3}$ (purple open squares) of the 160 nm-thick Mn_5Ge_3 film versus temperature. $S_{Ge} > 0$ and increases with temperature, while $S_{5/3} < 0$ and decreases when temperature increases. The opposite sign of S_{Ge} and $S_{5/3}$ confirms that the Mn_5Ge_3/Ge ohmic contact (Fig. 2b) is obtained between n-type metallic Mn_5Ge_3 and p-type semiconductor Ge (Fig. 2a). Electrons and holes are respectively the majority carriers in the Mn_5Ge_3 film and the Ge film, moving towards the colder region of the films. According to Hall effect measurements, the average carrier concentration in the Mn_5Ge_3 film is $\sim 2.0 \times 10^{20}$ cm^{-3}, while it is $\sim 9.0 \times 10^{18}$ cm^{-3} in the Ge film at room temperature. The

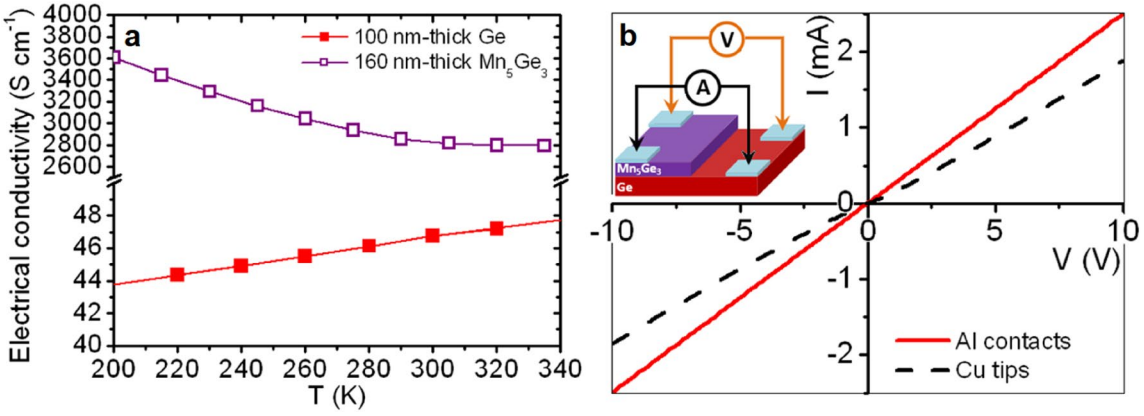

Figure 2. Electrical measurements performed on Ge and Mn_5Ge_3 thin films deposited by magnetron sputtering on glass substrate and crystallized by ex situ annealing. (**a**) Electrical conductivity of the Ge (solid squares) and Mn_5Ge_3 (open squares) films versus temperature. (**b**) I–V measurements performed on a Mn_5Ge_3-step/Ge-terrace structure (see inset) using Cu tips placed either directly on the films (dashed line) or on Al contacts sputtered on the films (solid line).

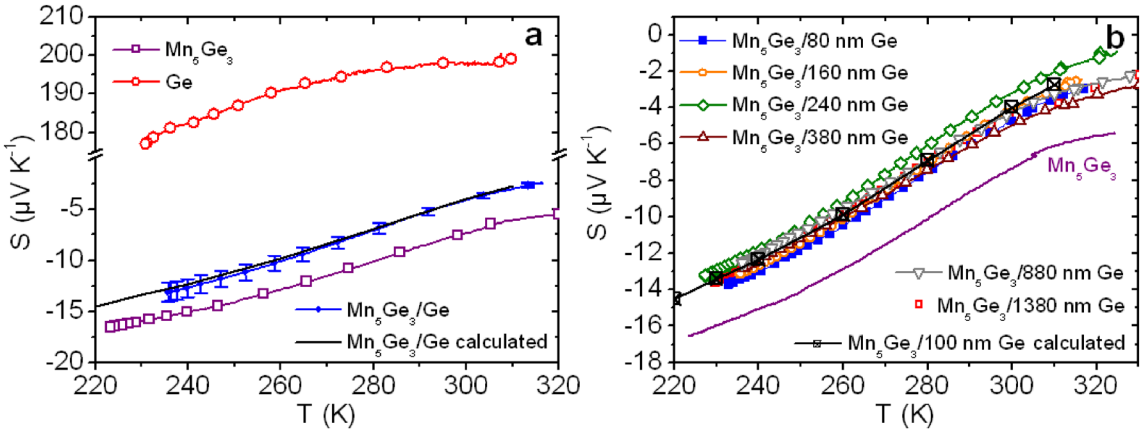

Figure 3. Seebeck coefficient measurements versus temperature performed on Mn_5Ge_3/Ge bilayers elaborated on glass substrate (see Fig. 4a). (**a**) Comparison of the Seebeck coefficient of a 160 nm-thick Mn_5Ge_3/100 nm-thick Ge bilayer (blue solid dots) with the Seebeck coefficient $S_{5/3}$ of a 160 nm-thick Mn_5Ge_3 film (purple open squares), S_{Ge} of a 100 nm-thick Ge film (red open circles), and the theoretical effective coefficient $S_{eff\text{-}th}$ of the bilayer (black solid line) calculated using the equation in Fig. 1e and the experimental values of $S_{5/3}$ and S_{Ge}, as well as of $\sigma_{5/3}$ and σ_{Ge} presented in Fig. 2a. (**b**) Comparison between the Seebeck coefficients of different Mn_5Ge_3/Ge bilayers made of a same 160 nm-thick Mn_5Ge_3 film in contact with a Ge film of different thickness, from 80 to 1380 nm. The purple solid line and the black crossed squares respectively correspond to $S_{5/3}$ and $S_{eff\text{-}th}$, also shown in (**a**).

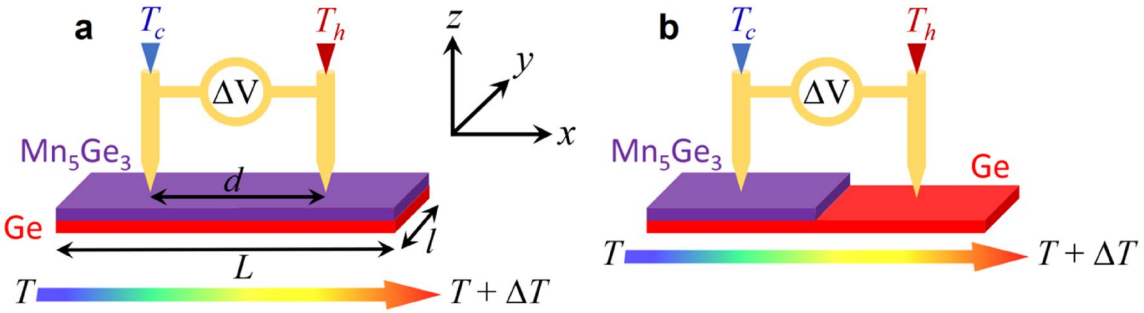

Figure 4. Schematics describing the two geometries used for Seebeck coefficient measurements aiming at investigating the Mn_5Ge_3/Ge interface contribution to the Seebeck coefficient in the case of parallel (**a**) or serial (**b**) charge carrier channels. In (**b**), the temperature gradient is applied in the direction x perpendicular to the Mn_5Ge_3-step.

carrier concentration is thus one order of magnitude smaller in the Ge film, while $|S_{Ge}|$ is more than one order of magnitude larger than $|S_{5/3}|$.

S_{Ge} and $S_{5/3}$ are compared in Fig. 3a with S_{eff} (blue dots) of the 160 nm-thick Mn_5Ge_3/100 nm-thick Ge bilayer measured according to the parallel-phase geometry. Figure 4a shows a schematic of experimental conditions. The value of S_{eff} is in between of those of S_{Ge} and $S_{5/3}$, but it is negative in the investigated temperature range and is close to $S_{5/3}$. $S_{eff\text{-}th}$ calculated using the equation given in Fig. 1e and the experimental values of σ_{Ge} and $\sigma_{5/3}$ (Fig. 2a) and of S_{Ge} and $S_{5/3}$ (Fig. 3a) versus temperature is also shown in Fig. 3a (black solid line). $S_{eff\text{-}th}$ is in very good agreement with experimental S_{eff}, showing no contribution of the Mn_5Ge_3/Ge interface. S_{eff} is closer to $S_{5/3}$ than to S_{Ge} due to $\sigma_{5/3} >> \sigma_{Ge}$ (Fig. 2a). Figure 3b presents the influence of the Ge layer thickness t_h on experimental S_{eff} compared to $S_{eff\text{-}th}$ calculated using experimental σ_{Ge} and S_{Ge} measured on a 100 nm-thick Ge film. The thickness of the Mn_5Ge_3 layer was kept constant (160 nm), while the thickness of the Ge layer was varied between 80 and 1380 nm in six different Mn_5Ge_3/Ge bilayers. All the measurements are close to $S_{eff\text{-}th}$, the maximum difference between S_{eff} and $S_{eff\text{-}th}$ at $T = 300$ K being 22% for example. Furthermore, no obvious dependence of the Ge thickness on S_{eff} could be determined, S_{eff} being closer to $S_{eff\text{-}th}$ in the sample with $t_h = 880$ nm than in the sample with $t_h = 240$ nm for example.

These results show that the interface between two polycrystalline thin films of Mn_5Ge_3 and Ge corresponding to an ohmic contact does not provide a conduction channel to charge carriers. The experimental S_{eff} of the Mn_5Ge_3/Ge bilayer can be predicted independently of layer thicknesses using the model of parallel conduction channels along the temperature gradient (Fig. 1e) for Ge and Mn_5Ge_3 layers thicker than 80 nm.

Mn_5Ge_3/Ge interface contribution to carrier filtering

In order to probe the contribution of the Mn_5Ge_3/Ge interface in the serial-phase geometry, S_{eff} was measured on Mn_5Ge_3/Ge bilayer samples exhibiting a step between the Mn_5Ge_3 layer and the Ge film as presented in Fig. 4b (Mn_5Ge_3-step/Ge-terrace structure). ΔV was measured across the Mn_5Ge_3 step while the Ge side of the sample was located either in the colder part or the hotter part (as in Fig. 4b) of the temperature gradient. Figure 5a presents the Seebeck coefficient measured versus temperature through the Mn_5Ge_3/Ge interface with the Ge side located either in the cold (blue open circles) or the hot region (orange open squares) of the temperature gradient. The Seebeck coefficient is different from the single films of Ge and Mn_5Ge_3, as well as from that measured on the Mn_5Ge_3/Ge bilayer (Fig. 5a), and cannot be reproduced using the regular equation of the serial-phase geometry given in Fig. 1f. Furthermore, at the same temperature, the Seebeck coefficient is different when charge carriers cross the interface from Ge-to-Mn_5Ge_3 (hot Ge) or from Mn_5Ge_3-to-Ge (cold Ge), showing clearly an impact of the interface on S_{eff}. S_{eff} exhibits higher values if the carriers move from hot Mn_5Ge_3 to cold Ge, and depending on the carrier direction through the interface, S_{eff} follows opposite variations versus temperature (increasing or decreasing versus temperature), exhibiting almost a symmetrical behavior around the value of ~ 30 μV K^{-1}. Figure 5b shows four consecutive Seebeck measurements performed on the same Mn_5Ge_3-step/Ge-terrace sample. The measurements are reproducible. However, few differences in the Seebeck values are observed between same-condition measurements (arrows in Fig. 5b), the interface influence on carriers displaying a stochastic character.

Figure 5c presents Seebeck measurements performed on two different Mn_5Ge_3-step/Ge-terrace samples. The global behavior of S_{eff} versus temperature is the same in the two samples depending on the carrier diffusion direction toward the interface. Though the values of the Seebeck coefficient are different for the two samples at the same temperature. S_{eff} is about 20 to 40 μV K^{-1} higher in the sample #2 (Fig. 5c). As shown in Fig. 1f, the effective Seebeck coefficient should obey $S_{eff} = \alpha\, S_{5/3} + (1-\alpha)\, S_{Ge}$ in the case of the Mn_5Ge_3/Ge serial-phase geometry. However, the bipolarity of the Ge film should be considered. Indeed, the Ge film being extrinsic, it contains two different charge carriers of significantly different concentrations: holes (h) and electrons (e), being respectively

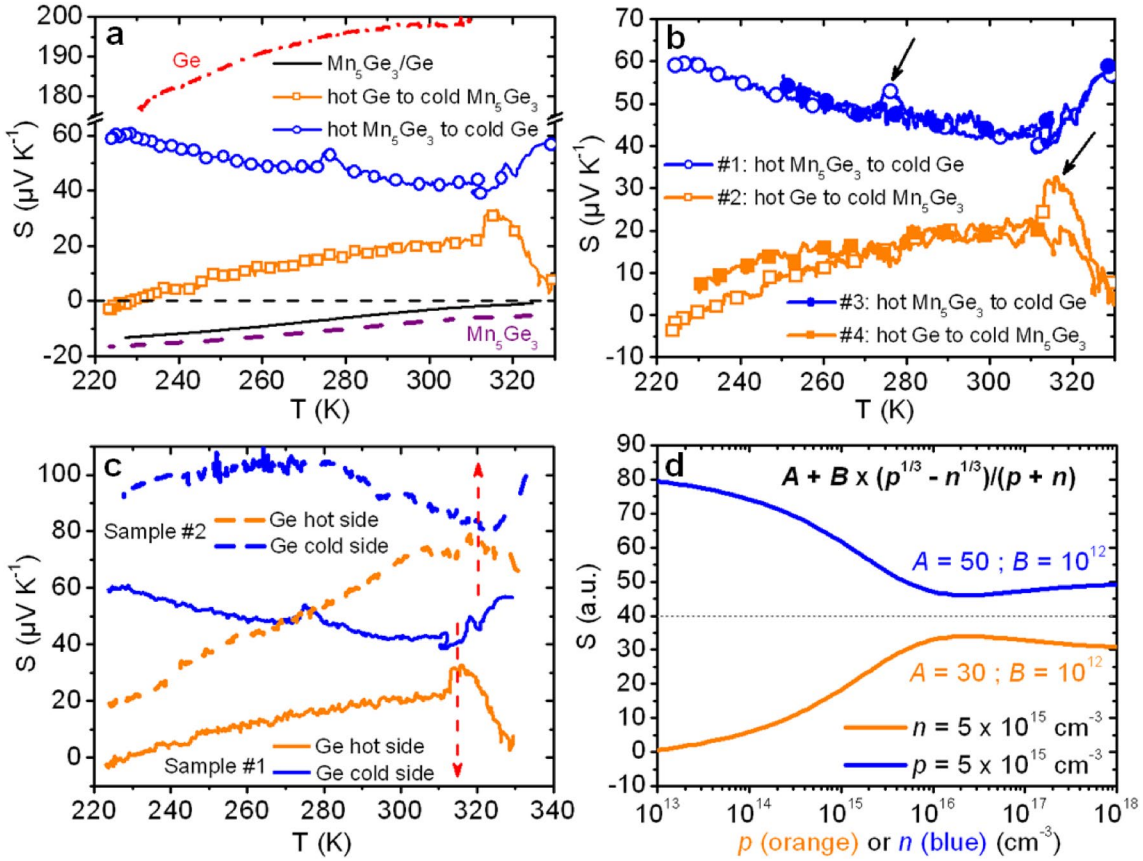

Figure 5. Seebeck coefficient variations versus temperature of Mn_5Ge_3-step/Ge-terrace structures (see Fig. 4b). (**a**) Seebeck coefficient measured for both cases: the Ge side placed in the hot (orange open squares) or in the cold (blue open circles) region of the temperature gradient, compared to the Seebeck coefficient of a single Mn_5Ge_3 (purple dashed line) or Ge (red dashed dotted line) film, and a Mn_5Ge_3/Ge bilayer (black solid line). (**b**) Four different measurements performed on a same Mn_5Ge_3-step/Ge-terrace sample, measurements #1 and #3 with Ge in the cold region of the temperature gradient, measurements #2 and #4 with Ge in the hot region of the temperature gradient. (**c**) Same measurements as in (**b**) but performed on two different Mn_5Ge_3-step/Ge-terrace samples. (**d**) Variations of the fraction $(p^{1/3} - n^{1/3})/(p+n)$ versus p (orange solid line) or n (blue solid line).

the majority and the minority charge carriers in the present case. Thus, a similar model as for the parallel-phase geometry should be used to consider the two conduction channels of holes and electrons in Ge, giving:

$$S_{eff} = \alpha S_{5/3} + (1-\alpha)\frac{S_h\sigma_h - S_e\sigma_e}{\sigma_h + \sigma_e} \quad (1)$$

With S_h and S_e the respective Seebeck coefficients of holes and electrons, and σ_h and σ_e their respective conductivities in the Ge film ($\sigma_{Ge} = \sigma_h + \sigma_e$). Typically, the coefficients α and $(1-\alpha)$ respectively correspond to the volume fractions of the two phases Mn_5Ge_3 and Ge in the considered bi-phase material. Though these coefficients should describe the volume difference of Mn_5Ge_3 and Ge crossed by the charge carriers between the two electrodes placed on the two sides of the Mn_5Ge_3 step considering the measurement geometry shown in Fig. 4b. According to Eq. (1), S_{eff} depends on (1) the position of the electrodes during measurement (i.e. the distance between the Mn_5Ge_3 step and the electrode located on the Ge terrace for example, Fig. 4b) through the coefficient α, (2) the variations of $S_{5/3}$ versus temperature, and (3) the Ge bipolarity versus temperature, without considering any interface effect.

The interface is an extended defect that can hold interfacial carrier traps, as well as carrier recombination centers[66–69]. Furthermore, the *n*-type Mn_5Ge_3/*p*-type Ge interface corresponds to an ohmic contact (Fig. 2b), and should provide carrier injection between Mn_5Ge_3 and Ge. Consequently, the interface can act as a sink (carrier recombination) or a source (carrier injection) of charge carriers in the Mn_5Ge_3 and Ge films depending on the carrier flux direction towards the Mn_5Ge_3/Ge interface. The Mn_5Ge_3/Ge interface is expected to locally modify the concentration of the charge carriers, and thus, to have a combined effect on the five parameters $S_{5/3}$, S_h, S_e, σ_h, and σ_e in Eq. (1), leading to complex variations of S_{eff} versus temperature, since temperature plays differently on carrier trapping/releasing, carrier recombination, and carrier injection. Neglecting the effect of the interface on the concentration of electrons in metallic Mn_5Ge_3, and assuming that the main effect of the interface is the modification of the hole concentration (p) and the electron concentration (n) in the semiconductor, one can roughly assume $S_h \propto p^{-2/3}$, $S_e \propto n^{-2/3}$[5–8,30,32,44], $\sigma_h \propto p$, and $\sigma_e \propto n$[6,30,55], leading to the approximation

$$S_{eff} \propto S_{Ge} \propto \frac{p^{1/3} - n^{1/3}}{p+n} \quad (2)$$

Figure 5d presents the variation of Eq. (2) either if p increases from 10^{13} to 10^{18} cm^{-3} while $n = 5\times10^{15}$ cm^{-3} (orange solid line) or if n increases from 10^{13} to 10^{18} cm^{-3} while $p = 5\times10^{15}$ cm^{-3} (blue solid line). The plot uses two arbitrary constant A and B according to $S = A + B\,(p^{1/3} - n^{1/3})/(p+n)$, which were adjusted in order to obtain Seebeck coefficient variations of the same order as those in Fig. 5c. The Seebeck coefficient variations with temperature suggested by Eq. (2) are not the same as the experimental variations reported in Fig. 5c, but show similar trends despite strong simplifications, particularly concerning p and n variations (Fig. 5d). The opposite variations of S_{eff} with opposite carrier diffusion directions toward the interface reported in Fig. 5 can be interpreted as mostly resulting from the modification of the charge carrier concentrations in Ge versus temperature due to the presence of the interface. S_{eff} variations when the charge carriers cross the interface from Mn_5Ge_3-to-Ge (cold Ge) can be interpreted as an increase of the fraction n/p versus T, while S_{eff} variations when the charge carriers cross the interface from Ge-to-Mn_5Ge_3 (hot Ge) can be interpreted as a decrease of the fraction n/p versus T.

Figure 6a presents a third type of measurements that was performed in order to support this interpretation. Two effective Seebeck coefficients were measured on a same Mn_5Ge_3-step/Ge-terrace sample while the temperature gradient was oriented along the Mn_5Ge_3 step. A first measurement was performed on the Mn_5Ge_3 step, and a second was performed on the Ge terrace. The first measurement should be similar to S_{eff} measured on Mn_5Ge_3/Ge bilayers (Fig. 3), and the second should correspond to S_{Ge} (red open circles in Fig. 3a) assuming no interface effect. Figure 6b shows four Seebeck coefficient measurements acquired sequentially versus temperature on the same Mn_5Ge_3/Ge bilayer. A first measurement was performed as described in Fig. 4a (black solid line), before the fabrication of a Mn_5Ge_3 step by chemical etching. $S_{eff} < 0$ in the investigated temperature range and its variations with temperature are similar to the previous measurements performed on similar samples, reported in Fig. 3. Then, a Mn_5Ge_3 step was made by chemical etching on the same sample, and S_{eff} was measured on the Mn_5Ge_3 step (blue open circles, $S_{eff} = \Delta V_1/\Delta T$ in Fig. 6a) and on the Ge terrace (red open squares, $S_{eff} = \Delta V_2/\Delta T$ in Fig. 6a) of the Mn_5Ge_3-step/Ge-terrace sample.

One can note that S_{eff} measured on the Mn_5Ge_3 step on the Mn_5Ge_3-step/Ge-terrace sample is slightly smaller than the measurements performed on the Mn_5Ge_3/Ge bilayer. In particular, S_{eff} change sign close to room temperature on the Mn_5Ge_3 step. According to the equation in Fig. 1e, the modification of S_{eff} can result from the modification of the four parameters $S_{5/3}$, S_{Ge}, $\sigma_{5/3}$, and σ_{Ge}. Consequently, the interpretation of this result is not straightforward, as it can result from carrier concentration variations in both Mn_5Ge_3 and Ge. Though the difference ΔS_{eff} between the Seebeck coefficients measured on the Mn_5Ge_3/Ge bilayer and on the Mn_5Ge_3 step on the Mn_5Ge_3-step/Ge-terrace sample at the same temperature is rather small: $\Delta S_{eff} < 5$ µV K^{-1}. In contrast, the Ge Seebeck coefficient measured on the Ge terrace of the Mn_5Ge_3-step/Ge-terrace sample is significantly smaller than that measured on the 100 nm-thick Ge film (red open circles in Fig. 3a). The interface has a strong effect on bipolar Ge as formerly suggested (Eq. 2). $S_{Ge} < 30$ µV K^{-1} in the Ge terrace of the Mn_5Ge_3-step/Ge-terrace sample in the investigated temperature range, corresponding to a decrease of S_{Ge} of about 160 µV K^{-1} with the presence of the interface. Finally, the Mn_5Ge_3 step was entirely removed by chemical etching, leaving only a Ge layer on the glass substrate and the Ge Seebeck coefficient was again measured on this sample (orange solid squares in Fig. 6b). A rather higher Ge Seebeck coefficient is recovered without the interface, with $S_{Ge} \geq 100$ µV K^{-1}. The fact that S_{Ge} is not as high as initially in the case of the unetched 100 nm-thick Ge film is attributed to an effect linked to the sequential chemical etching and sample annealing during the Seebeck measurements.

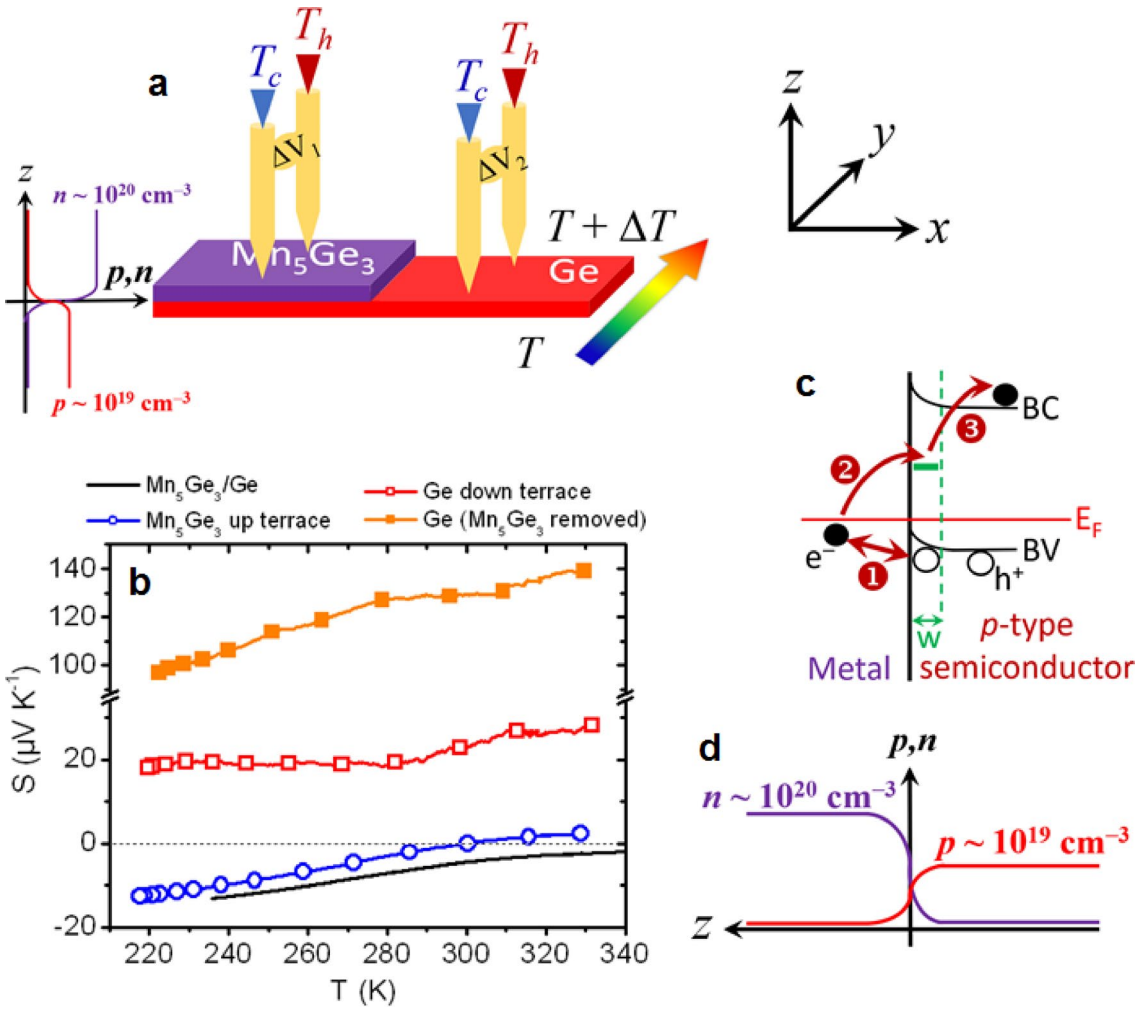

Figure 6. Seebeck coefficient measurements versus temperature performed on a same Mn_5Ge_3-step/Ge-terrace sample. (**a**) Schematic of the measurement geometry, the temperature gradient is applied in the direction *y* parallel to the Mn_5Ge_3-step. (**b**) Comparison between the Seebeck coefficients measured on the Mn_5Ge_3/Ge bilayer before the formation of the Mn_5Ge_3-step by chemical etching (black solid line, see Fig. 4a), and on both the Mn_5Ge_3 upper terrace (blue open circles, $\Delta V_1/\Delta T$ in **a**) and the Ge down terrace (red open squares, $\Delta V_2/\Delta T$ in (**a**) after the formation of the Mn_5Ge_3-step, and finally on the same Ge film once the Mn_5Ge_3 layer has been chemically removed (orange solid squares). (**c**) Schematic of the electronic band diagram at the Mn_5Ge_3/Ge interface during the Seebeck measurements sketched in (**a**). (**d**) Schematic illustrating the expected variations of the free electron concentration *n* and free hole concentration *p* through the Mn_5Ge_3/Ge interface, along the *z* direction (see also **a**).

Figure 6c shows a schematic of the expected electronic band diagram at the Mn_5Ge_3/Ge interface. The temperature gradient being oriented in the *y* direction during measurement (Fig. 6a), the electro-chemical potential at the interface between Mn_5Ge_3 and Ge should be at equilibrium at each position *y* along the temperature gradient. Nevertheless, because of the opposite types of the Mn_5Ge_3 (*n*-type) and Ge (*p*-type) films, a strong electron and hole concentration gradient should be present at the interface vicinity (Fig. 6d), which can act as the driving force for carrier injection and electron–hole recombination. For example, interfacial electron–hole recombination (mechanism (1) in Fig. 6c) should act as a sink of electrons in Mn_5Ge_3 and a sink of holes in Ge, while interfacial carrier injection should promote the injection of holes in Mn_5Ge_3 and the injection of electrons in the Ge valence band due to the ohmic property of the contact (mechanism (1) in Fig. 6c). Electron injection in the Ge conduction band due to the presence of defects at the interface is also possible depending on temperature (mechanisms (2) + (3) in Fig. 6c). However, the electron concentration in Mn_5Ge_3 being about one order of magnitude higher than the hole concentration in Ge according to Hall effect measurements (Fig. 6d), interfacial carrier injection and recombination are expected to have a stronger effect on the carrier concentrations in Ge, in agreement with the results displayed in Figs. 5 and 6b.

Outlook

The influence of the *n*-type Mn_5Ge_3/*p*-type Ge interface on the effective Seebeck coefficient of a Mn_5Ge_3/Ge bilayer has been investigated experimentally. The Mn_5Ge_3/Ge interface does not contribute to charge carrier

transport. However, this metal/semiconductor interface of ohmic character contributes to charge carrier filtering. The filtering effect results from carrier injection or recombination at the interface, which depends on the direction of the carrier flux. The charge carrier concentration in the metal being significantly higher than the charge carrier concentrations in the semiconductor, interfacial carrier injection and recombination have a stronger effect in the semiconductor. Consequently, the modification of the effective Seebeck coefficient of the multiphase material due to the presence of the interface is mainly driven by the change of carrier concentrations in the semiconductor. The Seebeck coefficient of the Mn_5Ge_3/Ge bi-phase material is driven by either an increase or a decrease of the fraction n/p in Ge, depending if the carrier flux respectively crosses the interface from Mn_5Ge_3-to-Ge or from Ge-to-Mn_5Ge_3. Ohmic metal/semiconductor interfaces alter the Seebeck coefficient of semiconductor–metal multiphase materials through carrier concentration filtering, mainly effective in the semiconductor volume.

Materials and methods

The Ge and Mn_5Ge_3 films were elaborated by magnetron sputtering and solid-state reactive diffusion. 99.99% pure Ge and 99.9% pure Mn targets were sputtered on $l = 1.5 \times L = 2.5$ cm^2 (Fig. 4a) glass substrates in a commercial magnetron sputtering system with a base vacuum of 10^{-8} Torr[55,58,59]. Ge and Mn deposition rates were calibrated by measuring the thickness of different films deposited in different conditions on oxidized Si substrate using X-ray reflectivity. The substrates were cleaned 10 min in an acetone bath before to be rinsed 10 min in alcohol in an ultrasonic cleaner. They were finally kept 30 min at 423 K in a baking furnace, before to be loaded in the sputtering chamber. Ge and Mn were deposited sequentially at room temperature on the glass substrates to form a Mn/Ge bilayer on the glass substrate. The samples were ex situ annealed at 400 °C for 10 min under vacuum ($P \sim 10^{-7}$ mbar) after deposition allowing for the growth of the Mn_5Ge_3 layer via reactive diffusion and the full crystallization of the Ge layer[55,59,70]. The thickness of the Mn layer was maintained the same for all the samples, while the thickness of the Ge film was varied in order to obtain a 160 nm-thick Mn_5Ge_3 layer on a Ge layer of different thicknesses. Hall measurements and sample resistivity were measured in the Van der Pauw geometry using a lab-made setup operating between 20 and 350 K. The applied magnetic field for Hall measurements was 0.5 T. The Seebeck coefficients of the films were measured using a home-made setup[48,53,55,71] between $T = 225$ and 325 K. The distance d between the two electrodes allowing to simultaneously determine the potential difference ΔV as well as the temperature gradient $\Delta T = T_h - T_c$ was 1 cm (Fig. 4a).

Data availability

All data are available in the main text.

Received: 13 September 2023; Accepted: 28 September 2023
Published online: 03 October 2023

References

1. Bell, L. E. Cooling, heating, generating power, and recovering waste heat with thermoelectric systems. *Science* **1979**(321), 1457–1461 (2008).
2. Shakouri, A. Recent developments in semiconductor thermoelectric physics and materials. *Annu. Rev. Mater. Res.* **41**, 399–431 (2011).
3. He, J. & Tritt, T. M. Advances in thermoelectric materials research: Looking back and moving forward. *Science (1979)* **357**, 635 (2017).
4. Xiao, Y. & Zhao, L.-D. Seeking new, highly effective thermoelectrics. *Science* **1979**(367), 1196–1197 (2020).
5. Fitriani, *et al.* A review on nanostructures of high-temperature thermoelectric materials for waste heat recovery. *Renew. Sustain. Energy Rev.* **64**, 635–659 (2016).
6. Gayner, C. & Kar, K. K. Recent advances in thermoelectric materials. *Prog. Mater. Sci.* **83**, 330–382 (2016).
7. Aswal, D. K., Basu, R. & Singh, A. Key issues in development of thermoelectric power generators: High figure-of-merit materials and their highly conducting interfaces with metallic interconnects. *Energy Convers. Manag.* **114**, 50–67 (2016).
8. Tan, G., Zhao, L.-D. & Kanatzidis, M. G. Rationally designing high-performance bulk thermoelectric materials. *Chem. Rev.* **116**, 12123–12149 (2016).
9. Binbin, J. *et al.* High figure-of-merit and power generation in high-entropy GeTe-based thermoelectrics. *Science* **377**, 208–213 (2022).
10. Gelbstein, Y., Rosenberg, Y., Sadia, Y. & Dariel, M. P. Thermoelectric properties evolution of spark plasma sintered (Ge 0.6Pb 0.3Sn0.1)Te following a spinodal decomposition. *J. Phys. Chem. C* **114**, 13126–13131 (2010).
11. Liu, *et al.* High-performance in n-type PbTe-based thermoelectric materials achieved by synergistically dynamic doping and energy filtering. *Nano Energy* **91**, 106706 (2022).
12. Komisarchik, *et al.* Solubility of Ti in thermoelectric PbTe compound. *Intermetallics* **89**, 16–21 (2017).
13. Kaller, M., Fuks, D. & Gelbstein, Y. Sc solubility in p-type half Heusler (Ti_{1-c} Sc_c)NiSn thermoelectric alloys. *J. Alloys Compd.* **729**, 446–452 (2017).
14. Gayner, C., Natanzon, Y. & Amouyal, Y. Effects of Co-doping and microstructure on charge carrier energy filtering in thermoelectric titanium-doped zinc aluminum oxide. *ACS Appl. Mater. Interfaces* **14**, 4035–4050 (2022).
15. Peng, Y. *et al.* Constructed Ge quantum dots and Sn precipitate SiGeSn hybrid film with high thermoelectric performance at low temperature region. *Adv. Energy Mater.* **12**, 2103191 (2022).
16. Liang, Z., Boland, M. J., Butrouna, K., Strachan, D. R. & Graham, K. R. Increased power factors of organic–inorganic nanocomposite thermoelectric materials and the role of energy filtering. *J. Mater. Chem. A Mater.* **5**, 15891–15900 (2017).
17. Hu, Q. *et al.* Realize high thermoelectric properties in n-Type Bi2Te2.7Se0.3/Y2O3 nanocomposites by constructing heterointerfaces. *ACS Appl. Mater. Interfaces* **13**, 38526–38533 (2021).
18. Fortulan, R. & Aminorroaya Yamini, S. Recent progress in multiphase thermoelectric materials. *Materials* **14**, 6059 (2021).
19. Peng, Y. *et al.* Improved thermoelectric property of B-doped Si/Ge multilayered quantum dot films prepared by RF magnetron sputtering. *Jpn. J. Appl. Phys.* **57**, 01AF03 (2018).
20. Park, W., Hwang, H., Kim, S., Park, S. & Jang, K.-S. Optimized thermoelectric performance of carbon nanoparticle-carbon nanotube heterostructures by tuning interface barrier energy. *ACS Appl. Mater. Interfaces* **13**, 7208–7215 (2021).
21. Khan, A. U. *et al.* Nano-micro-porous skutterudites with 100% enhancement in ZT for high performance thermoelectricity. *Nano Energy* **31**, 152–159 (2017).

22. Li, J.-F., Liu, W.-S., Zhao, L.-D. & Zhou, M. High-performance nanostructured thermoelectric materials. *NPG Asia Mater.* **2**, 152–158 (2010).
23. Martín-González, M., Caballero-Calero, O. & Díaz-Chao, P. Nanoengineering thermoelectrics for 21st century: Energy harvesting and other trends in the field. *Renew. Sustain. Energy Rev.* **24**, 288–305 (2013).
24. Nadtochiy, A. *et al.* Enhancing the Seebeck effect in Ge/Si through the combination of interfacial design features. *Sci. Rep.* **9**, 16335 (2019).
25. Karuppaiah, S., Beaudhuin, M. & Viennois, R. Investigation on the thermoelectric properties of nanostructured. *J. Solid State Chem.* **199**, 90–95 (2013).
26. Zamanipour, Z. *et al.* The effect of phase heterogeneity on thermoelectric properties of nanostructured silicon germanium alloy. *J. Appl. Phys.* **114**, 023705 (2013).
27. Zhang, X. *et al.* Significant enhancement in thermoelectric properties of half-Heusler compound TiNiSn by grain boundary engineering. *J. Alloys Compd.* **901**, 163686 (2022).
28. Wang, X. W. *et al.* Enhanced thermoelectric figure of merit in nanostructured n-type silicon germanium bulk alloy. *Appl. Phys. Lett.* **93**, 193121 (2008).
29. Kockert, M., Mitdank, R., Zykov, A., Kowarik, S. & Fischer, S. F. Absolute Seebeck coefficient of thin platinum films. *J. Appl. Phys.* **126**, 105106 (2019).
30. Wang, A. *et al.* High thermoelectric performance of Cu_2Se-based thin films with adjustable element ratios by pulsed laser deposition. *Mater. Today Energy* **24**, 100929 (2022).
31. Majumdar, A. Thermoelectricity in semiconductor nanostructures. *Science* **1979**(303), 777–778 (2004).
32. Mao, J., Liu, Z. & Ren, Z. Size effect in thermoelectric materials. *NPJ Quant. Mater.* **1**, 16028 (2016).
33. Mehta, R. J. *et al.* Seebeck tuning in chalcogenide nanoplate assemblies by nanoscale heterostructuring. *ACS Nano* **4**, 5055–5060 (2010).
34. Jeyakanthan, M. & Subramanian, U. Enhanced DC conductivity and Seebeck coefficient of $CoWO_4/PbWO_4$ nanocomposites: Role of interface. *Appl. Phys. A* **127**, 569 (2021).
35. Puneet, P. *et al.* Preferential scattering by interfacial charged defects for enhanced thermoelectric performance in few-layered n-type Bi_2Te_3. *Sci. Rep.* **3**, 3212 (2013).
36. Sun, J., Yu, J., Guo, Y. & Wang, Q. Enhancing power factor of SnSe sheet with grain boundary by doping germanium or silicon. *NPJ Comput. Mater.* **6**, 99 (2020).
37. Neophytou, N. *et al.* Simultaneous increase in electrical conductivity and Seebeck coefficient in highly boron-doped nanocrystalline Si. *Nanotechnology* **24**, 205402 (2013).
38. Hasezaki, K., Hamachiyo, T., Ashida, M., Ueda, T. & Noda, Y. Thermoelectric properties and scattering factors of finely grained Bi_2Te_3-related materials prepared by mechanical alloying. *Mater. Trans.* **51**, 863–867 (2010).
39. Lin, Y. *et al.* Expression of interfacial Seebeck coefficient through grain boundary engineering with multi-layer graphene nanoplatelets. *Energy Environ. Sci.* **13**, 4114–4121 (2020).
40. Narducci, D., Selezneva, E., Cerofolini, G., Frabboni, S. & Ottaviani, G. Impact of energy filtering and carrier localization on the thermoelectric properties of granular semiconductors. *J. Solid State Chem.* **193**, 19–25 (2012).
41. Kim, R. & Lundstrom, M. S. Computational study of energy filtering effects in one-dimensional composite nano-structures. *J. Appl. Phys.* **111**, 024508 (2012).
42. Singha, A. & Muralidharan, B. Incoherent scattering can favorably influence energy filtering in nanostructured thermoelectrics. *Sci. Rep.* **7**, 7879 (2017).
43. Lee, W.-Y. *et al.* Interface-induced seebeck effect in $PtSe_2/PtSe_2$ van der Waals Homostructures. *ACS Nano* **16**, 3404–3416 (2022).
44. Li, J., Wang, Y., Zhang, G., Chen, D. & Ren, F. First-principles investigation of the electronic structures and Seebeck coefficients of PbTe/SrTe interfaces. *J. Appl. Phys.* **125**, 035107 (2019).
45. Liu, D. *et al.* Anisotropic layered Bi_2Te_3-In_2Te_3 composites: Control of interface density for tuning of thermoelectric properties. *Sci. Rep.* **7**, 43611 (2017).
46. Santos, R., Nancarrow, M., Dou, S. X. & Aminorroaya Yamini, S. Thermoelectric performance of n-type Mg_2Ge. *Sci. Rep.* **7**, 3988 (2017).
47. Pallecchi, I. *et al.* Seebeck effect in the conducting $LaAlO_3/SrTiO_3$ interface. *Phys. Rev. B* **81**, 085414 (2010).
48. Oueldna, N. *et al.* Seebeck coefficient in multiphase thin films. *Mater. Lett.* **266**, 127460 (2020).
49. Sun, P. *et al.* Large Seebeck effect by charge-mobility engineering. *Nat. Commun.* **6**, 7475 (2015).
50. Hu, G., Edwards, H. & Lee, M. Silicon integrated circuit thermoelectric generators with a high specific power generation capacity. *Nat. Electron.* **2**, 300–306 (2019).
51. Dhawan, R. *et al.* Si0.97Ge0.03 microelectronic thermoelectric generators with high power and voltage densities. *Nat. Commun.* **11**, 4362 (2020).
52. Gharsallah, M. *et al.* Giant Seebeck effect in Ge-doped SnSe. *Sci. Rep.* **6**, 26774 (2016).
53. Portavoce, A. *et al.* Thermoelectric power factor of $Ge_{1-x}Sn_x$ thin films. *Materialia* **14**, 100873 (2020).
54. Ma, H. *et al.* First-principle predictions of the electric and thermal transport performance on high-temperature thermoelectric semiconductor MnTe2. *J. Alloys Compd.* **898**, 162813 (2022).
55. Portavoce, A., Assaf, E., Bertoglio, M., Narducci, D. & Bertaina, S. Magnetic moment impact on spin-dependent Seebeck coefficient of ferromagnetic thin films. *Sci. Rep.* **13**, 172 (2023).
56. Nishimura, T., Nakatsuka, O., Akimoto, S., Takeuchi, W. & Zaima, S. Crystalline orientation dependence of electrical properties of Mn Germanide/Ge(1 1 1) and (0 0 1) Schottky contacts. *Microelectron. Eng.* **88**, 605–609 (2011).
57. Sellai, A. *et al.* Barrier height and interface characteristics of $Au/Mn_5Ge_3/Ge$ (1 1 1) Schottky contacts for spin injection. *Semicond. Sci. Technol.* **27**, 035014 (2012).
58. Portavoce, A. *et al.* Ferromagnetic MnCoGe thin films produced via magnetron sputtering and non-diffusive reaction. *Appl. Surf. Sci.* **437**, 336–346 (2018).
59. Abbes, O., Portavoce, A., Le Thanh, V., Girardeaux, C. & Michez, L. Phase formation during Mn thin film reaction with Ge: Self-aligned germanide process for spintronics. *Appl. Phys. Lett.* **103**, 172405 (2013).
60. Assaf, E., Portavoce, A., Hoummada, K., Bertoglio, M. & Bertaina, S. High Curie temperature Mn_5Ge_3 thin films produced by non-diffusive reaction. *Appl. Phys. Lett.* **110**, 072408 (2017).
61. Khelidj, H. *et al.* Ge(Sn) growth on Si(001) by magnetron sputtering. *Mater. Today Commun.* **26**, 101915 (2021).
62. Sellai, A. *et al.* Barrier height and interface characteristics of Au/Mn $_5$ Ge $_3$ /Ge (1 1 1) Schottky contacts for spin injection. *Semicond. Sci. Technol.* **27**, 035014 (2012).
63. Spiesser, A., Saito, H., Jansen, R., Yuasa, S. & Ando, K. Large spin accumulation voltages in epitaxial Mn_5Ge_3 contacts on Ge without an oxide tunnel barrier. *Phys. Rev. B* **90**, 205213 (2014).
64. Cain, T. A. *et al.* Seebeck coefficient of a quantum confined, high-electron-density electron gas in $SrTiO_3$. *Appl. Phys. Lett.* **100**, 161601 (2012).
65. Takashima, R., Shiomi, Y. & Motome, Y. Nonreciprocal spin Seebeck effect in antiferromagnets. *Phys. Rev. B* **98**, 020401(R) (2018).
66. Joshi, D. P. Carrier recombination at grain boundaries in polycrystalline silicon under optical illumination. *Solid-State Electron.* **29**, 19–24 (1986).

67. Joshi, D. P. & Bhatt, D. P. Theory of grain boundary recombination and carrier transport in polycrystalline silicon under optical illumination. *IEEE Trans. Electr. Dev.* **37**, 237–249 (1990).
68. Gaury, B. & Haney, P. M. Charged grain boundaries and carrier recombination in polycrystalline thin-film solar cells. *Phys. Rev. Appl.* **8**, 054026 (2017).
69. Pierret, R. F. *Advanced Semiconductor Fundamentals* (Addison-Wesley Publishing Company, 1989).
70. Assaf, E., Portavoce, A., Hoummada, K., Bertoglio, M. & Bertaina, S. High Curie temperature of Mn_5Ge_3 thin films produced by non-diffusive reaction. *Appl. Phys. Lett.* **110**, 7 (2017).
71. Oueldna, N. *et al.* Seebeck coefficient variations of α-MgAgSb in crystalline Mg-Ag-Sb thin films. *J. Alloys Compd.* **932**, 167692 (2023).

Acknowledgements
The authors would like to thank Prof Dario Narducci from the University of Milano-Bicocca for Hall effect and electrical measurements and interesting discussions.

Author contributions
A.P.: conceptualization, methodology, investigation, visualization, funding acquisition, project administration, supervision, writing—original draft, writing—review & editing. S.H.: investigation, writing—review & editing. M.B.: investigation, resources, writing—review & editing.

Competing interests
The authors declare no competing interests.

Additional information
Correspondence and requests for materials should be addressed to A.P.

Reprints and permissions information is available at www.nature.com/reprints.

Publisher's note Springer Nature remains neutral with regard to jurisdictional claims in published maps and institutional affiliations.